

Symmetry indicators vs. bulk winding numbers of topologically non-trivial bands

Alexander C. Tyner¹ and Pallab Goswami^{1,2}

¹ *Graduate Program in Applied Physics, Northwestern University, Evanston, Illinois, 60208, USA and*

² *Department of Physics and Astronomy, Northwestern University, Evanston, Illinois 60208, USA*

(Dated: September 15, 2021)

The symmetry-indicators provide valuable information about the topological properties of band structures in real materials. For inversion-symmetric, non-magnetic materials, the pattern of parity eigenvalues of various Kramers-degenerate bands at the time-reversal-invariant momentum points are generally analyzed with the combination of strong Z_4 , and weak Z_2 indices. Can the symmetry indicators identify the tunneling configurations of $SU(2)$ Berry's connections or the three-dimensional, winding numbers of topologically non-trivial bands? In this work, we perform detailed analytical and numerical calculations on various effective tight-binding models to answer this question. If the parity eigenvalues are regarded as fictitious Ising spins, located at the vertices of Miller hypercube, the strong Z_4 index describes the net ferro-magnetic moment, which is shown to be inadequate for identifying non-trivial bands, supporting even integer winding numbers. We demonstrate that an "anti-ferromagnetic" index, measuring the staggered magnetization can distinguish between bands possessing zero, odd, and even integer winding numbers. The coarse-grained analysis of symmetry-indicators is substantiated by computing the change in rotational-symmetry-protected, quantized Berry's flux and Wilson loops along various high-symmetry axes. By simultaneously computing ferromagnetic and anti-ferromagnetic indices, we categorize various bands of bismuth, antimony, rhombohedral phosphorus, and Bi_2Se_3 .

I. INTRODUCTION:

Classification of non-trivial topology in a solid-state system of N bands requires analysis of a corresponding $N \times N$ Hermitian matrix. It is common practice to consider only the ground state wavefunction when proceeding with topological classification, formed by the Slater determinant of eigenfunctions, $\psi_n(\mathbf{k})$, such that $E_n(\mathbf{k}) < E_F$, where E_F is the Fermi energy^{1–11}. However, this procedure immediately comes into question when we consider that the Fermi energy, or more generally the chemical potential, is non-universal. Moreover, exotic surface states are accepted as ‘smoking gun’ evidence of topological order. For a Hamiltonian, $H(\mathbf{k})$, surface states are the result of solving the Schrodinger equation $H(-i\nabla)\Psi(\mathbf{x}) = E\Psi(\mathbf{x})$, with specific open boundary conditions (OBCs). Through the imposition of OBCs, translation symmetry is broken and bands are no longer well defined. The structure of surface states depends on the entire Hilbert space, and the bulk Fermi energy or chemical potential takes on no meaning other than to be a helpful reference. In order to provide a comprehensive topological description of the band-structure and bulk-boundary correspondence, one must consider all bands in the Hilbert space.

Symmetry-indicator methods for diagnosis of topology in a given band structure rely on identification of patterns in the assignment of symmetry eigenvalues. For non-magnetic materials preserving space-inversion symmetry the pattern of parity eigenvalues play the most important role for identifying band topology. While commonly applied to the ground state, we emphasize that these methods provide greater insight when applied to individual bands. In the current literature, symmetry indicators have achieved remarkable success, especially when combined with high-throughput screening techniques^{3,4,7,12–22}. Most famously, the Fu-Kane strong topological insulator (STI) index for a given band, recently elevated from a \mathbb{Z}_2 to a \mathbb{Z}_4 index (denoted as κ_1), classifies ferromagnetic moment of parity eigenvalues on the Miller cube, when considering the parity eigenvalues as fictitious Ising spins (or net monopole moment when parity eigenvalues are treated as positive and negative charges). A perfect ferromagnetic (FM) configuration, one in which all parity eigenvalues are equal ($\kappa_1 = \pm 4$), and an anti-ferromagnetic (AFM) Néel configuration (or 2^d multipole configuration), one in which there exists an equal number of positive and negative parity eigenvalues ($\kappa_1 = 0$), are considered trivial and topologically equivalent. This provides the basic idea of what is a topologically trivial band. Notably, for the AFM configuration, all weak TI indices are trivial as well. All other configurations have been proposed to be in correspondence with either a STI or weak TI¹². Symmetry based analysis can be further substantiated by use of Wilson loops^{23–29}. In addition, K-theory based classification has been extended in terms of equivariant K-theory³⁰ and Atiyah-Hirzebruch spectral sequence³¹.

Can an anti-ferromagnetic configuration of parity eigenvalues correspond to a genuinely trivial system? Obviously, the net ferromagnetic moment is not the appropriate tool for recognizing Néel configuration. A new indicator is needed to quantify the staggered moment of parity eigenvalues. In this paper, we therefore formulate a staggered index, denoted by κ_{AF} . We show in simple models of d -dimensional first-order topological insulators, classified by d -th spherical homotopy group $[\pi_d(S^d) = \mathbb{Z}]$, κ_{AF} is directly related to the bulk winding number. The Néel configuration leads to the maximal winding number, $|\kappa_{AF}| = 2^{d-1}$. For $d = 3$, bulk winding numbers have a direct relationship with the Chern-Simons invariant of $SU(2)$

Berry's connections. Computation of the Chern-Simons invariant is generally considered to be impractical in many-band tight-binding (TB) models and *Ab initio* data, despite its relevance in a wide range of systems such as the recently proposed class of chiral higher-order topological insulators (HOTIs)³². In order to substantiate the connection between κ_{AF} and third-homotopy we perform a joint analysis of planar Wilson loops (PWL)^{33,34} and Wilson lines (WLs)²³⁻²⁹. For a single band to support a three dimensional winding number, we must be able to identify linked, closed curves supporting a π Berry's phase^{4,6,35,36}; PWLs and WLs identify closed curves of π non-Abelian Berry's phase in-plane and along cycles of the Brillouin zone (BZ) respectively, accommodating linking.

The topological significance of AFM ordering demonstrated by κ_{AF} , further calls for a revision of κ_1 . Prior to imposition of the \mathbb{Z}_4 condition, a single band supporting $\kappa_1 = 0$ (AFM configuration) and $\kappa_1 = \pm 4$ (FM configuration) must be made distinct. Only then application of κ_1 and κ_{AF} , not to the ground state, but to each band in the Hilbert space individually, can provide a comprehensive view of topology from the standpoint of parity eigenvalues. In the context of real materials, we detail how this analysis calls into question best practices for low-energy modeling of a topological many-band system. As an example, in Fig. (1), the low-energy band structure of bismuth (Bi), antimony (Sb), phosphorus (P), and bismuth selenide (Bi_2Se_3) is shown with bands color coded according to classification under κ_1 . It is clear there is an immediate obstacle to producing an appropriate low energy model, as the valence and conduction bands closest to the Fermi energy admit distinct κ_1 . We emphasize that understanding a many band system is a problem of embedding upon classifying the individual bands.

The organization of this paper is as follows. In section II, we carry out a rigorous classification of analytically tractable TB models of two and four Kramers pairs. This analysis informs the origin of a non-vanishing Chern-Simons invariant, and shortcomings of the current symmetry indicator methods. Explicit details regarding the formulation and application of κ_{AF} are then provided. We choose to begin by working with simplified TB models in order to simulate each type of band that will be encountered in the subsequent analysis of more complicated systems. In section III, *Ab initio* data of bismuth is studied in detail. The topology of bismuth, once thought to be trivial due to Fu-Kane classification of the ground state, has received renewed interest with claims that the bulk supports TCI and HOTI phases. We demonstrate that these classifications, based on application of symmetry indicators to the ground state wavefunction, overlook many important topological features. In section IV, antimony, phosphorus, and bismuth selenide are surveyed in further depth using κ_{AF} and κ_1 . Classification of the ground state for P and Bi (Sb and Bi_2Se_3) using the STI index leads to the conclusion that they are topologically equivalent. We elucidate that the individual bands in these systems are distinct and that this must be taken into account if experimental data of surface states is to be properly interpreted. Finally, we close by providing a summary of the current work as well as an outlook on the technical developments required to improve third-homotopy classification of many-band systems.

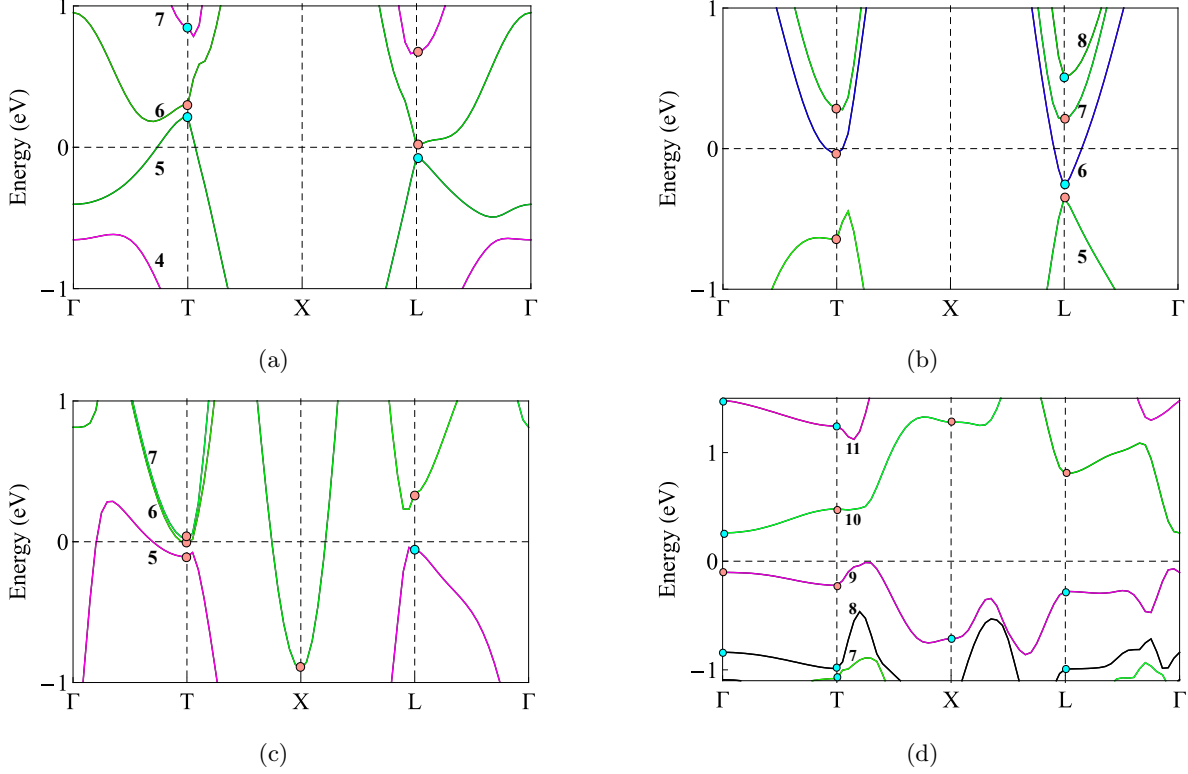


FIG. 1: Low energy band structure of (a) bismuth, (b) antimony, (c) phosphorus and (d) bismuth selenide; detailing the distinct topology of the bands which lie nearest to the Fermi energy. The bands are colored according to classification via κ_1 . Green bands correspond to $\kappa_1 = \pm 1, \pm 3$, purple bands to $\kappa_1 = \pm 2$, blue bands to $\kappa_1 = 0$ as a result of an even number of positive and negative parity eigenvalues, and black bands to $\kappa_1 = \pm 4$ prior to imposition of the \mathbb{Z}_4 condition (i.e. all parity eigenvalues are of same sign). The parity eigenvalues at the TRIM locations are labeled with cyan(light-red) dots corresponding to eigenvalue -1(+1). The bands are also numbered in accordance with their appearance in Figs. (8b), (12a), (13a), and (14a), respectively. Computational details can be found in Sec. III and IV.

II. WINDING NUMBERS AND THE ANTI-FERROMAGNETIC INDEX

For gaining analytical insight into third-homotopy classification of $SU(2)$ connections and its relationship with symmetry indicators, we will first employ a tight-binding model of two Kramers degenerate bands with cubic symmetry, written as $H(\mathbf{k}) = \sum_{j=1}^4 d_j(\mathbf{k})\Gamma_j$, where Γ_j 's are 4×4 anti-commuting matrices, given explicitly as $\Gamma_{j=1,2,3} = \tau_1 \otimes \sigma_j$ and $\Gamma_4 = \tau_3 \otimes \sigma_0$ where $\sigma_{0,1,2,3}(\tau_{0,1,2,3})$ are the 2×2 identity matrix and three Pauli matrices respectively. We then define,

$$d_{j=1,2,3}(\mathbf{k}) = t_p \sin k_j, \quad d_4(\mathbf{k}) = t_s \left(\Delta - \delta_1 \sum_{j=1}^3 \cos k_j - \delta_2 \sum_{i<j=1}^3 \cos k_i \cos k_j - \delta_3 \prod_{j=1}^3 \cos k_j \right), \quad (1)$$

where $t_{p,s}$ are hopping parameters with units of energy and $\Delta, \delta_1, \delta_2, \delta_3$ are dimensionless band parameters. For simplicity the lattice constant has been set to unity. Parity(inversion) symmetry is generated by $\mathcal{P} = \Gamma_4$ such that $\mathcal{P}^\dagger H(\mathbf{k}) \mathcal{P} = H(-\mathbf{k})$. At the time-reversal invariant momentum (TRIM) points, the parity operator commutes with the Hamiltonian, allowing us to label individual bands via parity eigenvalues ± 1 . The TRIM points can be considered as the corners of a cube with axes corresponding to the three reciprocal lattice vectors, which we refer to as the Miller cube. Each TRIM point can be written as,

$$Q_{\nu_1, \nu_2, \nu_3} = \frac{1}{2} (\nu_1 \mathbf{b}_1 + \nu_2 \mathbf{b}_2 + \nu_3 \mathbf{b}_3), \quad (2)$$

where $(\nu_1 \nu_2 \nu_3)$ are the Miller indices which can take on values $\nu_j = 0, 1$ and \mathbf{b}_j are the reciprocal lattice vectors. For the simple cubic system the reciprocal lattice vectors are orthogonal, and thus the BZ and Miller cube have the same geometry. This will not be true in general, however, one can always consider the Miller cube via the mapping provided by the Miller indices.

A preliminary analysis of bulk-topology for the ground state involves calculation of the strong and weak indices. The strong index, ν_0 is calculated by multiplying the inversion eigenvalues of all occupied Kramers pairs at each of the TRIM locations, with the result expressed as $(-1)^{\nu_0}$ ⁷. Correspondingly, $\nu_0 = +1(0)$ indicates that the system is topological(trivial). The weak indices apply a similar classification to the two-dimensional planes of the Miller cube which do not include the Γ point. Recently, it was shown by Khalaf et. al^{12,14}, that the strong index can be elevated from a Z_2 invariant to a Z_4 invariant, denoted κ_1 , where

$$\kappa_1 = \frac{1}{4} \sum_K (n_K^+ - n_K^-), \quad (3)$$

and $n_K^+ (n_K^-)$ is the number of occupied bands with even (odd) parity at each TRIM point, K. Through a careful choice of band parameters in eq. (1), as depicted in Fig. (2b), the ten distinct phases shown in Fig. (3a) and (3b), distinguished via parity eigenvalue analysis of the valence band, can be realized.

Due to the cubic symmetry of the TB model, each C_4 symmetric plane defined by $k_j = 0, \pi$ acts as a mirror plane supporting a mirror Chern number, C_m . The two-fold symmetric planes defined by $k_i = k_j$ also support mirror symmetry, but we will focus our attention on the C_4 planes. Second homotopy classification can be accomplished by calculating the mirror Chern number of the valence band in the $k_z = 0, \pi$ planes. This is calculated explicitly as,

$$C_m(k_z) = \frac{1}{4\pi} \iint_{-\pi}^{\pi} \tilde{\mathbf{d}}(\mathbf{k}) \cdot \left(\partial_{k_x} \tilde{\mathbf{d}}(\mathbf{k}) \times \partial_{k_y} \tilde{\mathbf{d}}(\mathbf{k}) \right) dk_x dk_y, \quad (4)$$

where $\tilde{\mathbf{d}}(\mathbf{k}) = \{d_1(\mathbf{k}), d_2(\mathbf{k}), d_4(\mathbf{k})\} / \sqrt{d_1(\mathbf{k})^2 + d_2(\mathbf{k})^2 + d_4(\mathbf{k})^2}$. This has been done for each of the ten phases with the results shown in Fig. (3a) and (3b). Of the ten phases, we note that seven support distinct values of quantized Berry's flux in the $k_z = 0, \pi$ planes, setting up a flux tunneling configuration. Importantly, each phase defined by $\kappa_1 = \pm 2$ lacks a flux tunneling configuration, with equivalent values of flux in all C_4 mirror planes. Phase IX proves to be of particular interest as this phase admits only trivial classification via the strong and weak TI indices while supporting flux tunneling. In sec. IV we demonstrate that the existence of such a band is not limited to simple TB models but can be identified in the known strong topological insulator, Bi_2Se_3 .

After determining second homotopy for high-symmetry planes, we are prepared to address the question of third homotopy classification, $\pi_3(S^3)$. This is accomplished by computing the three-dimensional winding number,

$$n_3 = \frac{1}{2\pi^2} \int_{BZ} d^3k \epsilon^{abcd} \hat{d}_a \partial_{k_x} \hat{d}_b \partial_{k_y} \hat{d}_c \partial_{k_z} \hat{d}_d. \quad (5)$$

For the present model, n_3 will be equal to the difference in mirror Chern number between $k_z = 0, \pi$ mirror planes. When this flux tunneling occurs, then there will be mutual linking between closed contours in the xy planes supporting π Berry's phase.

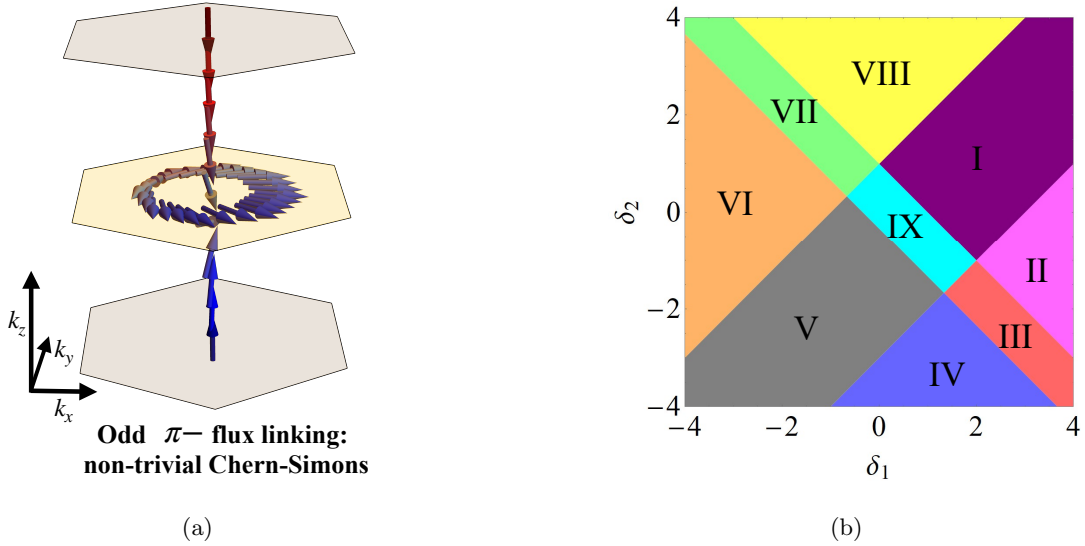


FIG. 2: (a) The closed curves of π -Berry's phase are shown using arrows to illustrate the π phase accrued by the eigenfunctions upon parallel transport along them. The closed curve lying in the plane, and the vertical line (forming a closed curve due to the periodic boundary conditions of the Brillouin zone) form a linking configuration. (b) Phase diagram corresponding to parity configurations seen in Fig. (3a) and (3b), for the tight-binding model of eq.(1), upon fixing $\Delta = 1$ and $\delta_3 = 2$.

It is clear that phases supporting $\kappa_1 = \pm 1, 3$, support an odd value of n_3 due to a flux tunneling configuration in which a single plane supports non-vanishing $|2\pi|$ flux. Interestingly, n_3 is even for phases in which the number of positive and negative parity eigenvalues are equal ($\kappa_1 = 0$). This is a direct result of the $k_j = 0, \pi$ planes supporting equal and opposite magnitudes of Berry's flux. *This observation emphasizes the need for modification of κ_1 to accommodate the in-equivalence of a vanishing result due to an overall canceling of parity eigenvalues and parity monopole configuration.* Finally, phases supporting $\kappa_1 = \pm 2$ do not support a flux tunneling configuration, yielding $n_3 = 0$.

More generally, the correspondence between flux tunneling and n_3 , as well as the connection between n_3 and parity eigenvalues can be understood in the following manner. At three-dimensions, an $O(4)$ vector field can support instanton or tunneling configurations which are classified by the third homotopy group, $\pi_3(S^3) = \mathbb{Z}$. The corresponding topological invariant is given by eq. (5). This winding number can be tied

to the change in second homotopy classification of the $O(3)$ vector field defined at the mirror planes. Since $SU(2)$ is equivalent to S^3 , from the $O(4)$ unit vector we can construct non-trivial classes of $SU(2)$ matrices, $U = \hat{d}_4\sigma_0 + i\hat{d}_j\sigma_j$. At the TRIM points, $\hat{d} = \{0, 0, 0, \pm 1\}$. Accordingly, the $SU(2)$ matrix becomes $\pm\sigma_0$, which are the two center elements of the $SU(2)$ group. The parity eigenvalues precisely describe the pattern of non-trivial Ising valued center elements on the Miller hypercube. The pattern of Ising spins on the Miller cube can be captured by defining different order parameters or symmetry indices. The net ferromagnetic moment is captured by κ_1 . A homotopically trivial configuration with $n_3 = 0$ corresponds to $\kappa_1 = \pm 4$, when all parity eigenvalues are the same. Are all $\kappa_1 = 0$ configurations topologically trivial? This can not be addressed without considering a different order parameter. For example, consider the extreme case of perfect Néel configuration of parity eigenvalues. The proper index for identifying this configuration will be the staggered magnetization, $\kappa_{AF} = \pm 4$, where

$$\kappa_{AF} = -\frac{1}{2} \sum_K (-1)^{(m+l+j)} \delta_K, \quad (6)$$

m, l, j are the Miller indices corresponding to TRIM location K and δ_K is the parity eigenvalue at K . This indicates that $\kappa_1 = 0$ configurations can have non-trivial topological classification in terms of even integer winding numbers.

In the vicinity of the TRIM points, $d_{i=1,2,3}$ take the form of hedgehogs, $\{\hbar v_1 k_1, \hbar v_2 k_2, \hbar v_3 k_3\}$. The hedgehog charge, given by the sign of the velocity parameters $\text{sgn}(v_1 v_2 v_3)$, is captured by κ_{AF} through inclusion of the term $(-1)^{(m+l+j)}$. The actual three-dimensional winding number is given by,

$$n_3 = \sum_K n_3^K, \quad n_3^K = -\frac{1}{2} \text{sgn}(v_1^K v_2^K v_3^K \delta_K). \quad (7)$$

This is the reason winding number can be tied exactly to κ_{AF} for the model given in eq. (1). This correspondence will not always be exact without accounting for n -fold rotational symmetry which can impact the hedgehog strength, as shown in the subsequent section, however, determination of winding number as even, odd, or vanishing will always be in direct correspondence. The only genuine topologically trivial state has perfect ferromagnetic arrangement with $\kappa_1 = \pm 4$ and $\kappa_{AF} = 0$.

For a general $SU(2)$ gauge connection, $\mathbf{A}(\mathbf{k})$, the Chern-Simons invariant term is given by,

$$CS = \frac{1}{4\pi} \int_{BZ} d^3k \epsilon^{ijk} \text{Tr} \left[A_i \partial_j A_k + \frac{2i}{3} A_i A_j A_k \right]. \quad (8)$$

Using the $SU(2)$ matrix U , we can define flat, or curvature-free, connections $\mathbf{A}(\mathbf{k}) = -iU^\dagger \nabla U$ for which $CS = 2\pi n_3$. When we work with the tight-binding model defined by eq. (1), the gauge connection for two-fold degenerate valence band has the meron form $A_-(\mathbf{k}) = \frac{-i}{2} U^\dagger \nabla U$, leading to $CS_- = CS/2$. If we perform a gauge transformation, $A'(\mathbf{k}) = g^\dagger A(\mathbf{k}) g - ig^\dagger \nabla g$, Chern-Simons invariant changes as

$$CS' = CS - \frac{1}{4\pi} \int_{BZ} d^3k \epsilon^{ijk} \text{Tr} \left[G_i \partial_j G_k + \frac{2i}{3} G_i G_j G_k \right], \quad (9)$$

where $\mathbf{G}(\mathbf{k}) = -ig^\dagger \nabla g$. Therefore if $CS = n\pi$, with $n \in \mathbb{Z}$, it can be changed to $CS' = n'\pi$ only through large gauge transformations with an $SU(2)$ matrix, g , possessing winding number $n_3 = (n' - n)$. If there

is a phase admitting $CS = 2n\pi$, it can be converted to zero only through an $SU(2)$ matrix with $n_3 = 2n$. For example, phase I and phase V both support a strong TI invariant $\nu_0 = 1$, and weak invariants $(0, 0, 0)$. However, these phases are distinguished by three dimensional winding number, when treated as a \mathbb{Z} valued object. Similar, phase II and phase VI cannot be distinguished via the strong or weak invariants. They can only be distinguished via n_3 . In more complex tight-binding models and *Ab initio* data it is not always feasible to implement eq. (8). For this reason, it becomes important to rely on symmetry data, and gauge invariant eigenvalues of Wilson loops.

Let us consider a high-symmetry line joining two TRIM points. Since this is a non-contractible cycle of the Brillouin zone, it is equivalent to S^1 . The Hamiltonian along any such high-symmetry line represents a map from S^1 to S^1 . Such maps can be classified by the first homotopy group, $\pi_1(S^1) = \mathbb{Z}$. For the current model $\pi_1(S^1) = 0, \pm 1$. Any odd integer winding will manifest as π Berry's phase. WLs quantify this winding by measuring the non-Abelian Berry phase accrued upon parallel transport between two identified points, (k_i and k_f) in the BZ and are calculated as,

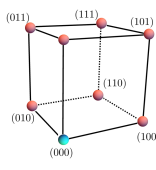
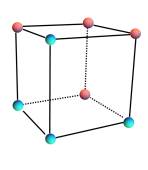
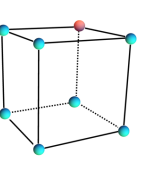
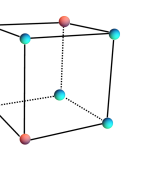
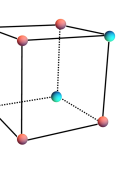
$$W_{n,j} = \mathcal{P} \exp \left[i \int_{k_i}^{k_f} A_{j,n}(\mathbf{k}) dk_j \right], \quad (10)$$

defining $A_{j,n}(\mathbf{k}) = -i\psi_{n,s}^\dagger(\mathbf{k})\partial_j\psi_{n,s'}$, where $\psi_{n,s}(\mathbf{k})$ are the eigenfunctions of the n -th band, with $s = \pm 1$ denoting the Kramers index, \mathcal{P} indicates path-ordering and $\partial_j = \frac{\partial}{\partial k_j}$. Wannier center charges (WCCs), \bar{j} , follow as eigenvalues of $\text{Im}(\text{Ln}(W_{n,j}))/ (2\pi)$. When calculated as a function of the transverse momenta, gapless points in the spectra of WCCs correspond to locations supporting lines of π Berry's phase. As the BZ is a three torus ($S^1 \times S^1 \times S^1$), this line of π Berry's phase is actually a closed curve along a single cycle of the torus admitting a non-trivial $\pi_1(S^1)$. Similarly PWL, can be used in high-symmetry planes to detect quantized flux and closed contours supporting π Berry's phase. These tools can thus be used in tandem to determine the presence of flux tunneling and linked curves of π Berry's phase. In order to exemplify robustness of these concepts in many-band systems and the impact of higher skyrmion numbers, we will now turn to a TB model proposed by Schindler et. al³⁷.

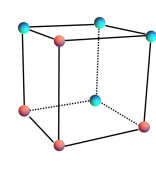
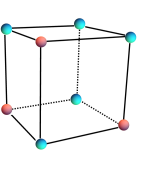
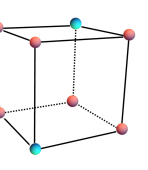
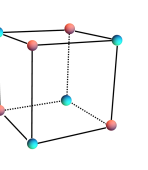
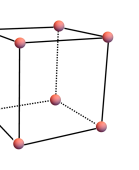
Eight band model of bismuth: Schindler et. al³⁷ have put forth an idealized, tight-binding model of four Kramers pairs, which is claimed to be topologically equivalent to bismuth (Bi). The Bloch Hamiltonian is succinctly written as,

$$H(\mathbf{k}) = \begin{bmatrix} H_{TB,I}(\mathbf{k}) + \epsilon & \delta M_{TB}(\mathbf{k}) \\ \delta M_{TB}(\mathbf{k})^\dagger & H_{TB,II}(\mathbf{k}) - \epsilon \end{bmatrix}, \quad (11)$$

demonstrating that the model consists of two topological insulators, $H_{TB,I/II}(\mathbf{k})$, coupled by the mass matrix $M_{TB}(\mathbf{k})$. For explicit details please consult the supplementary information of Schindler et. al³⁷. The first BZ of this model is designed to align with the first BZ of bismuth when considering the conventional unit cell and is shown in Fig. (4a). The main symmetries of this model are parity, time-reversal, and three-fold rotation about the z -axis although, when isolated, $H_{TB,I/II}(\mathbf{k})$ support six-fold rotational symmetry about the z -axis. The band structure, using the band parameters defined in the appendix of Schindler et. al³⁷, is shown in Fig. (4b). The parity, \mathcal{P} and three-fold rotation operator, C_{3z} , for $H(\mathbf{k})$ follow as $\mathcal{P} = \mathcal{P}_I \oplus \mathcal{P}_{II}$

Phase	I	II	III	IV	V
Parity Eigenvalues					
$(\kappa_1; \nu_1, \nu_2, \nu_3)$	(3;000)	(0;111)	(-3;111)	(-2;111)	(1;000)
$C_m(k_z = \pi) - C_m(k_z = 0)$	(-1)-(0)=-1	(-1)-(+1)=-2	(+1)-(0)=+1	(+1)-(+1)=0	(+2)-(-1)=+3
n_3	+1	-2	+1	0	+3
κ_{AF}	-1	+2	-1	0	-3

(a)

Phase	VI	VII	VIII	IX	X
Parity Eigenvalues					
$(\kappa_1; \nu_1, \nu_2, \nu_3)$	(0;111)	(-1;111)	(2;111)	(0;000)	(4;000)
$C_m(k_z = \pi) - C_m(k_z = 0)$	(+1)-(-1)=+2	(+1)-(-2)=+3	(-1)-(-1)=0	(+2)-(-2)=0	(0)-(0)=0
n_3	+2	+3	0	+4	0
κ_{AF}	-2	-3	0	-4	0

(b)

FIG. 3: Upon fixing $\delta_{1,2}$ according to the phase diagram in Fig. (2b), the valence band of the model in eq. (1) realizes the above configurations for parity eigenvalues. In phase I the corners of the Miller cube are labeled by the corresponding Miller indices. Each corner corresponds to a TRIM location of the Brillouin zone. Parity eigenvalue +1(-1) is indicated by red(cyan) sphere. We calculate the parity eigenvalue index κ_1 and the weak TI indices, $\nu_{i=1,2,3}$ for each configuration. Each of these indices conveys information regarding the ferromagnetic ordering of parity eigenvalues on the Miller cube. In order to illustrate the correspondence between a tunneling configuration of quantized Berry's flux and third homotopy, n_3 , the mirror Chern number C_m is computed in the $k_z = 0, \pi$ planes with the difference shown to be equivalent to n_3 in each case. Finally, correspondence between n_3 and the anti-ferromagnetic ordering of parity eigenvalues on the Miller cube is shown by computing κ_{AF} in each case.

and $C_{3z} = C_{3z,I} \oplus C_{3z,II}$, where $\mathcal{P}_j(C_{3z,j})$ is the parity(three-fold rotation) operator for $H_{TB,j}(\mathbf{k})$, given by Schindler et. al. As a result we can tabulate the Fu-Kane index for each Kramers pair, as well as the sum of parity eigenvalues $\kappa_{1,n}$. The results of this tabulation are shown in Tab. (4c) along with the C_{3z} eigenvalues of each Kramers pair along the z -axis.

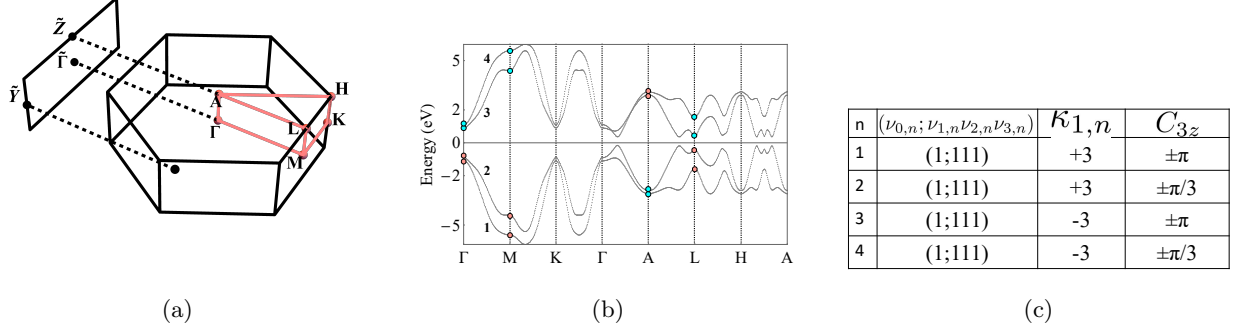


FIG. 4: (a) Schematic of bulk and (100) surface Brillouin zone for tight-binding model given by Eq. (11). TRIM points are labeled. The bulk band structure along the high symmetry path shown in red is detailed in (b). Parity eigenvalues at TRIM locations are labeled with red(cyan) corresponding to +1(-1). (c) Results of symmetry indicator analysis for each individual Kramers pair as well as the C_{3z} eigenvalues, $e^{\pm i\pi/3}$ or $e^{\pm i\pi}$, supported by each Kramers pair along the z -axis.

It is immediately clear that both occupied Kramers pairs support a non-trivial strong TI index. As a result the strong index of the ground state is trivialized ($\nu_{0,occ} = 0$), however κ_1 , which has been shown to be stable against the addition of bands admitting $\nu_{0,n} = +1$, yields the non-trivial result of $\kappa_{1,occ} = 2$ ^{12,14,16,19}. Schindler et. al, make a further argument for the non-trivial nature of this model by demonstrating that the occupied Kramers pairs can be separated into two sub-spaces based on their C_{3z} eigenvalues. Calculating the strong index in each subspace we find $\nu_0^{\pi/3} = \nu_0^\pi = +1$, consistent with the proposed symmetry indicator analysis for Bi in the main body of their work.

Band	$xy_\Gamma : C_{\mathcal{R}}$	$xy_A : C_{\mathcal{R}}$
1	0	+3
2	0	+1
3	0	-3
4	0	-1

TABLE I: Relative Chern number for each of the four Kramers degenerate bands in tight-binding model given by eq. (11), using parameters detailed in the supplementary material of Schindler et. al³⁷, setting $\delta = 0$ such that no mixing occurs between $H_{TB,I/II}(\mathbf{k})$. Bands are labeled by their energy at the Γ point, i.e. $E_1(0) < E_2(0) < E_3(0) < E_4(0)$. We note that bands 1 and 3(2 and 4) correspond to

$$H_{TB,II}(\mathbf{k})(H_{TB,I}(\mathbf{k})).$$

In correspondence with our analysis of the cubic models, we focus our attention on the individual high-symmetry planes at $k_z = 0$ (xy_Γ plane) and $k_z = \pi/c$ (xy_A plane), calculating quantized Berry's flux for each Kramers pair. We begin by setting $\delta = 0$, such that there is no mixing between $H_{TB,I/II}(\mathbf{k})$. Following the gauge fixing procedure outlined in Tyner et. al³³, the relative Chern number, $C_{\mathcal{R}} = \theta_m/(2\pi)$, can be directly calculated with a definite sign for each Kramers pair, labeled by their energy at the Γ point, i.e. $E_1(0) < E_2(0) < E_3(0) < E_4(0)$. The results of this calculation are listed in Tab. I. We note that $H_{TB,I}(\mathbf{k})$ introduces higher-harmonics that elevate the skyrmion number in each plane without effecting the parity eigenvalue structure.

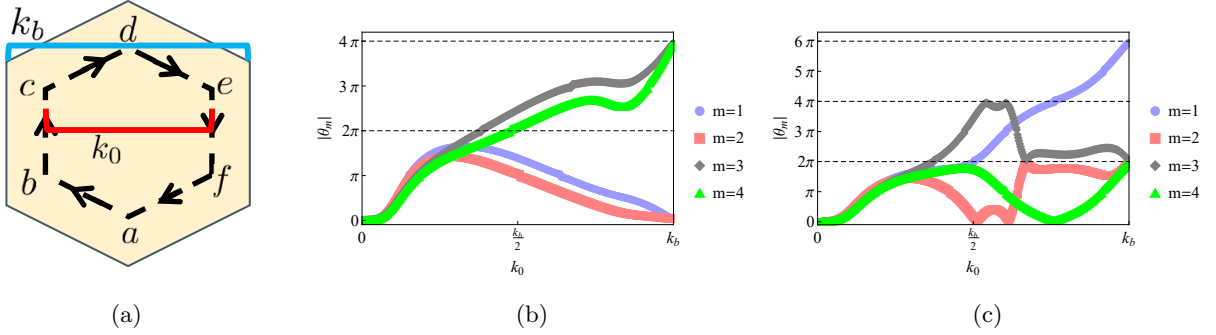


FIG. 5: (a) Schematic of the path-ordered, closed curve around which the planar Wilson loop is calculated in the xy_Γ and xy_A planes for the tight-binding model given in eq. (11), utilizing the band parameters given in the appendix of Schindler et. al³⁷. The yellow region represents the first Brillouin zone in the xy planes, and the closed curve is parameterized by k_0 , such that when $k_0 = k_b$, the path encloses the full Brillouin zone. (b) Results of planar Wilson loop in the xy_Γ plane for each band, m . As opposed to the situation in which mixing between $H_{TB,I/II}(\mathbf{k})$ is removed by setting $\delta = 0$, bands 3 and 4 now support a quantized, non-vanishing flux. (c) Results of planar Wilson loop in the xy_A plane. Once again the magnitude of flux has been altered as a result of including mixing between $H_{TB,I/II}(\mathbf{k})$.

We now reintroduce the mass matrix, which has the effect of lowering the rotational symmetry of the z -axis from 6-fold to 3-fold. In addition, by using the parameters laid out in Schindler et. al³⁷, we are working in the strong mixing limit, $|\delta| > |\epsilon|$. The magnitude of the resulting non-Abelian flux is computed via PWL. The PWL is defined as,

$$W_n = \mathcal{P}\exp \left[i \oint \sum_{j=1}^2 A_{j,n}(\mathbf{k}(l)) \frac{dk_j}{dl} dl \right], \quad (12)$$

and describes the $SU(2)$ Berry's phase accrued by the n -th wavefunction upon parallel transport along a closed, non-interacting curve C , lying in the xy plane, parameterized by $\mathbf{k}(l)$. As an element of the $SU(2)$ group, upon integration, W_n can be written as, $W_n(C) = \exp \left[i\theta_n \hat{\Omega} \cdot \sigma \right]$, where the gauge invariant angle θ_n can be related to the magnitude of non-Abelian Berry's flux through a non-Abelian generalization of a stokes theorem. The results of the PWL calculation as a function of the area enclosed by the closed path is shown in Fig. (5). In order to assign a definite sign to the magnitude of the flux and define the relative

Chern number unambiguously for each band, an Abelian gauge fixing procedure is implemented. The relative Chern number, $C_{\mathcal{R}} = \theta_m/(2\pi)$ of each band is listed in Table II. Full details of this calculation are given in the methods section.

Band	$xy_{\Gamma} : C_{\mathcal{R}}$	$xy_A : C_{\mathcal{R}}$
1	0	+3
2	0	-1
3	+2	-1
4	-2	-1

TABLE II: Relative Chern number for each of the four Kramers degenerate bands in tight-binding model given by eq. (11), using parameters detailed in the supplementary material of Schindler et. al³⁷. As a result of the mixing between the two constituent topological insulators, $H(\mathbf{k})_{TB.I/II}$, in Eq. (11), the magnitude of non-Abelian flux is modified from the results in Tab. I.

This result demonstrates that we can no longer rely on angular momentum alone to identify the magnitude of non-Abelian flux when mixing between distinct C_{3z} sub-spaces is allowed, as band 2 and 3 have each undergone a change in magnitude equivalent to $\pm 2\pi$ respectively. If this system were to fall in the weak mixing limit, $|\delta| < |\epsilon|$, prior analysis of the decoupled model would have remained valid. Further, this situation demonstrates the complexity associated with deducing skyrmion number in a many band system without rigorous calculation. Nevertheless, it is important to emphasize that the flux tunneling configuration supported by each Kramers pair is unaffected, i.e. the difference in magnitude of quantized flux between the two high-symmetry planes remained exactly the same value as it was when $\delta = 0$. As a result, both application of κ_{AF} to individual bands, as well as the magnitude of flux tunneling will remain invariant.

In order to provide a more complete comparison with the cubic models analyzed previously, the four-band tight-binding models, $H_{TB,I/II}(\mathbf{k})$, can be isolated and modified as detailed below to simulate bands supporting various values of κ_1 . For simplicity we refer to bands supporting $\kappa_{1,n} = \pm 1, \pm 3$ as class A, $\kappa_{1,n} = \pm 2$ as class B and $\kappa_{1,n} = 0$ as class C. Each TB model can be decomposed as, $H_{TB,l}(\mathbf{k}) = \sum_{j=1}^4 d_j^l \Gamma_j$, where Γ_j 's are 4×4 mutually anti-commuting matrices defined explicitly as, $\Gamma_{j=1,2} = \tau_1 \otimes \sigma_j$, $\Gamma_3 = \tau_2 \otimes \sigma_0$, $\Gamma_4 = \tau_3 \otimes \sigma_0$ where $\sigma_{j=0,1,2,3}(\tau_{j=0,1,2,3})$ are the 2×2 identity matrix and Pauli matrices respectively.

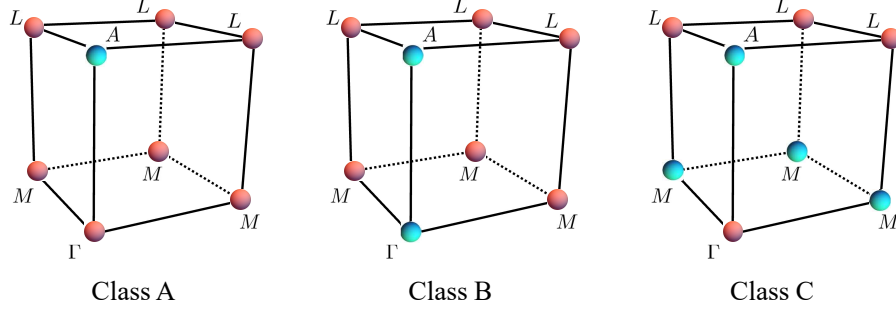


FIG. 6: Parity eigenvalues at TRIM locations for valence band of $H_{TB,I/II}(\mathbf{k})$, upon modification to simulate class A, B, and C bands of bismuth as determined from *Ab initio* data. Cyan and light-red spheres indicate parity eigenvalues -1 and +1 respectively.

Class A bands: As the valence/conduction bands of $H_{TB,I/II}(\mathbf{k})$ admit $\kappa_{1,n} = \mp 3$, they can be used as written by Schindler et. al³⁷.

Class B bands: In order to simulate this structure, we will adjust the band parameter $m_{I/II}$ such that $m_{I/II} = 0.25$. As a result, parity eigenvalues at the Γ point are inverted, matching those at the A point, yielding $\kappa_{1,n} = \pm 2$ for the valence and conduction Kramers pairs respectively.

Class C bands:: In order to simulate this structure, we modify d_4^l as given by Schindler et. al³⁷, to the form,

$$d_4^l \rightarrow m_l + t_1 \cos \mathbf{k} \cdot \mathbf{a}_3 (\cos \mathbf{k} \cdot \mathbf{a}_1 + \cos \mathbf{k} \cdot \mathbf{a}_2 + \cos \mathbf{k} \cdot (\mathbf{a}_1 + \mathbf{a}_2)), \quad (13)$$

where the lattice vectors \mathbf{a}_j are given by Schindler et. al³⁷, and we have set $2m_l = t = 1$. In this construction, the parity eigenvalues at the Γ and L points are of one sign while parity eigenvalues at A and M points are of opposite sign for each Kramers pair, yielding $\kappa_{1,n} = 0$.

After making the above modifications, third-homotopy classification can be carried out by computing the $O(4)$ winding number. The results of this calculation are then be compared to the calculated magnitude of flux in the xy_Γ and xy_A plane as well as κ_{AF} . This is done in Fig. (7). We note the correspondence that emerges between flux tunneling, κ_{AF} , and n_3 .

Class A	$xy_\Gamma : C_{\mathcal{R}}$	$xy_A : C_{\mathcal{R}}$	n_3	κ_{AF}
$H_{TB,I}(\mathbf{k})$	0	1	1	-1
$H_{TB,II}(\mathbf{k})$	0	3	3	-1
Class B	$xy_\Gamma : C_{\mathcal{R}}$	$xy_A : C_{\mathcal{R}}$	n_3	κ_{AF}
$H_{TB,I}(\mathbf{k})$	1	1	0	0
$H_{TB,II}(\mathbf{k})$	3	3	0	0
Class C	$xy_\Gamma : C_{\mathcal{R}}$	$xy_A : C_{\mathcal{R}}$	n_3	κ_{AF}
$H_{TB,I}(\mathbf{k})$	-1	1	2	-2
$H_{TB,II}(\mathbf{k})$	-3	3	6	-2

FIG. 7: Upon modification of $H_{TB,I/II}(\mathbf{k})$ to simulate class A, B and C bands, the relative Chern number is calculated for the valence band in the $xy_{\Gamma,A}$ planes. The $O(4)$ winding number is then computed following eq. (5) to determine the third-homotopy classification. We can conclude from these results that class A, B, and C bands admit odd, zero and even values of n_3 respectively, which is captured by the anti-ferromagnetic index. The precise magnitude of n_3 can be determined from the magnitude of flux tunneling.

III. APPLICATION TO *AB INITIO* DATA

Topological analysis of *Ab initio* data presents a significantly more complex challenge than simple TB models. In particular, third homotopy classification beyond the \mathbb{Z}_2 valued axion angle is extremely challenging from first-principles^{32,38–40}. It is imperative to tackle *Ab initio* data as even realistic tight-binding models such as the celebrated sixteen band Liu-Allen model, struggle to properly capture the topology of a many band system^{41,42}. Bismuth is selected as it is one of the preeminent materials in the study of topological order with $\text{Bi}_{1-x}\text{Sb}_x$ serving as the first experimentally realized topological insulator⁴³. Despite being labeled topologically trivial under a Fu-Kane \mathbb{Z}_2 classification, application of newly-refined symmetry indicators have led to proposals that the bulk admits both higher-order and rotationally protected crystalline topology^{37,44–49}. Our analysis uncovers that all bands of bismuth are topologically non-trivial with k_z axis serving as a flux tunneling configuration between the high-symmetry xy planes. This novel tunneling configuration underpins the diversity of topological phases that can be realized by studying Bi as a function of buckled honeycomb layers^{50–59}.

Model and symmetries: Bulk Bi has a rhombohedral structure, given by space group R_{3m} , leading to a 3D bulk BZ in the shape of truncated octahedron⁶⁰. The bulk band structure along the high-symmetry path is shown in Fig. (9), with the n -th Kramers pair labeled by its energy at the Γ point, i.e $E_n(0) < E_{n+1}(0)$.

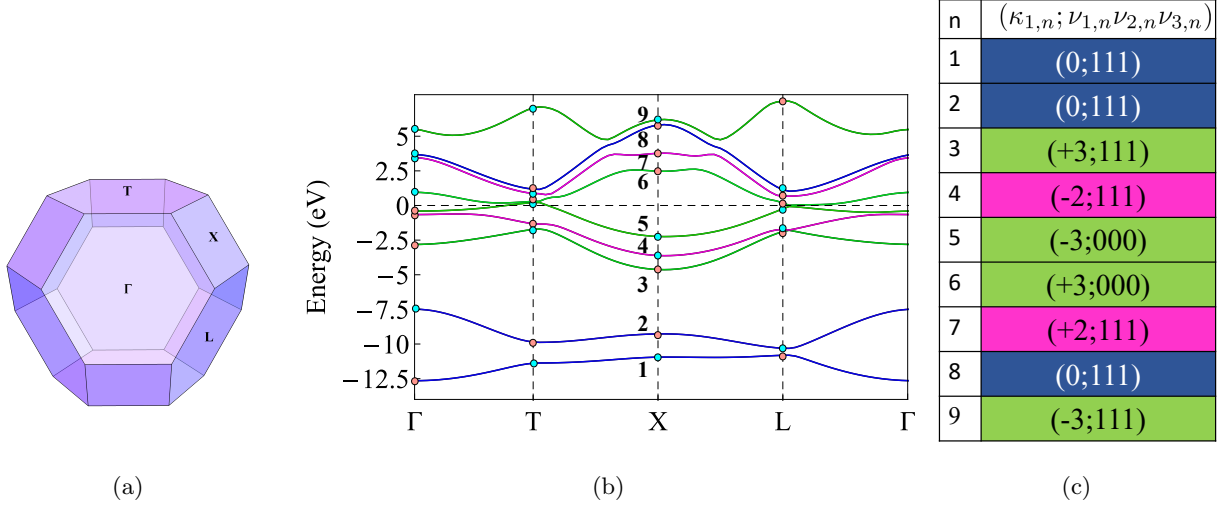


FIG. 8: (a) The bulk Brillouin zone of Bi is in the shape of a truncated octahedron with high-symmetry points labeled. (b) Bulk band structure of Bi along high symmetry path. Light-red(cyan) dots indicate parity eigenvalues +1(-1) at TRIM points. Bands are colored according to classification outlined in (c). (c) Fu-Kane strong index ($\nu_{0,n}$) and sum of parity eigenvalues ($\kappa_{1,n}$ index) for each Kramers degenerate band leads to formation of three distinct classes. Class A, colored green, supports non-trivial $\nu_{0,n} = +1$. Class B, colored purple, supports trivial $\nu_{0,n}$ and non-trivial $\kappa_{1,n} \neq 0$. Class C, colored blue, is trivial according to both $\nu_{0,n}$ and $\kappa_{1,n}$.

The primitive reciprocal lattice vectors follow as,

$$\mathbf{b}_1 = (-1, -\sqrt{3}/3, b)g, \quad (14)$$

$$\mathbf{b}_2 = (1, -\sqrt{3}/3, b)g, \quad (15)$$

$$\mathbf{b}_3 = (0, 2\sqrt{3}/3, b)g, \quad (16)$$

where $b = 0.384919$ and $g = 1.36307\text{\AA}^{-1}$ is a reciprocal lattice vector constant⁶¹. The time reversal invariant momenta are defined as,

$$Q_{(n_1, n_2, n_3)} = \frac{1}{2}(n_1\mathbf{b}_1 + n_2\mathbf{b}_2 + n_3\mathbf{b}_3), \quad (17)$$

where,

$$\Gamma = Q_{(0,0,0)}, L = \{Q_{(1,0,0)}, Q_{(0,1,0)}, Q_{(0,0,1)}\}, T = Q_{(1,1,1)}, X = \{Q_{(1,1,0)}, Q_{(0,1,1)}, Q_{(1,0,1)}\}. \quad (18)$$

The primary symmetries include three-fold rotational symmetry about the $[111]$ axis (C_{3z}), two-fold rotational symmetry about the $[\bar{1}10]$, $[10\bar{1}]$, and $[01\bar{1}]$ axes (C_2), inversion symmetry (\mathcal{I}), and mirror planes $\mathcal{M}_{1\bar{1}0}$, $\mathcal{M}_{10\bar{1}}$, and $\mathcal{M}_{01\bar{1}}$. Each layer along the (111) axis forms a buckled honeycomb lattice. All first principles based on density-functional theory (DFT) are carried out using the Quantum Espresso software package^{62–64}. Exchange-correlation potentials use the Perdew-Burke-Ernzerhof (PBE) parametrization of the generalized

gradient approximation (GGA)⁶⁵. The Wannier90 and Z2pack software packages were utilized in calculation of all topological invariants^{26,27,66}.

First principles calculations demonstrate that, for the five occupied bands, $k_1 = -2$. It is this result which has been used to propose that Bi supports non-trivial topology beyond the paradigm of the Fu-Kane index^{37,44–48}. In order to provide a more detailed perspective, $\nu_{j,n}$ and κ_1 are tabulated for each individual Kramers pair, n , as seen in Fig. (8c). From this information, we group the bands into the three classes: A, B, and C, as designated in the prior section. We emphasize that *the result $\kappa_1 = -2$ for the ground state is not a result of the two occupied bands which support a non-trivial strong TI invariant (3 and 5), but instead as a result of band 4 which supports $\kappa_1 = -2$* . This brings into question the proper low energy modeling required to accurately capture the topology of Bi. The model of Schindler et. al³⁷, eq. (11), attempts to simulate Bi with two occupied Kramers pairs that support a non-trivial strong TI invariant, however, an argument could easily be made that a model with the topology of phase II in Fig. (3a) is more appropriate. Such questions elucidate the difficulty in modeling the topological nature of the ground state, and instead the necessity of simulating individual Kramers pairs and subsequently understanding the effects of embedding into a many band system.

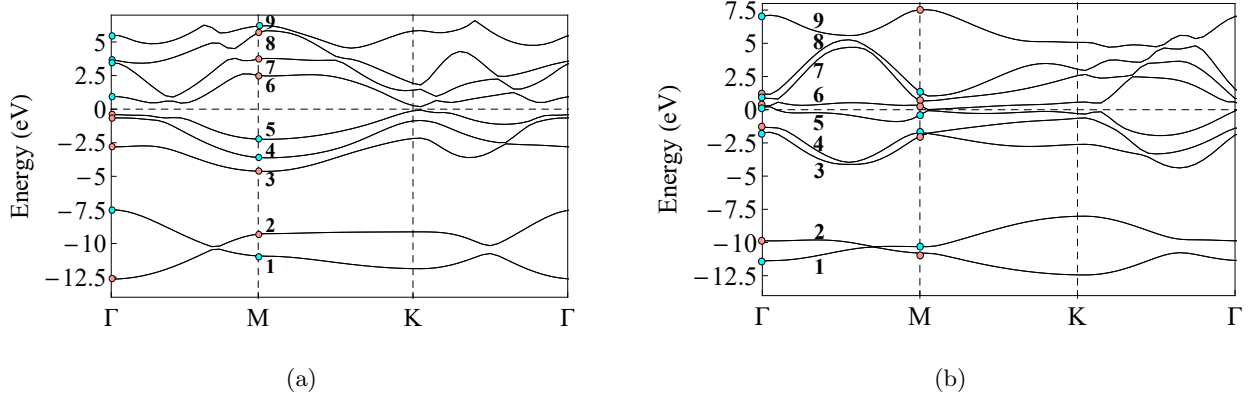


FIG. 9: (a,b) Band structure of Bi in the xy_Γ and xy_T planes respectively along the high symmetry path $\Gamma - M - K - \Gamma$. Light-red(cyan) dots indicate parity eigenvalues $+1(-1)$ at TRIM points.

To aid in the identification of flux tunneling, we analyze the embedded xy planes centered at the 3D Γ (xy_Γ plane) and T points (xy_T plane) supporting three-fold rotational symmetry. These planes support their own set of TRIM locations, listed in Table III. The band structure in the $xy_{\Gamma,T}$ planes along high symmetry

Γ	M	K
$\mathbf{k} = (0, 0)$	$\mathbf{k} = (\mathbf{b}_2 - \mathbf{b}_1)/2$	$\mathbf{k} = (\mathbf{b}_3 + \mathbf{b}_2 - 2\mathbf{b}_1)/3$

TABLE III: High symmetry points of $xy_{\Gamma,T}$ planes.

lines are shown in Fig. (9a)-(9b). The Hamiltonian at both the Γ and M points commute with the parity operator, allowing us to label the bands by their inversion eigenvalues. We note that both class B and C

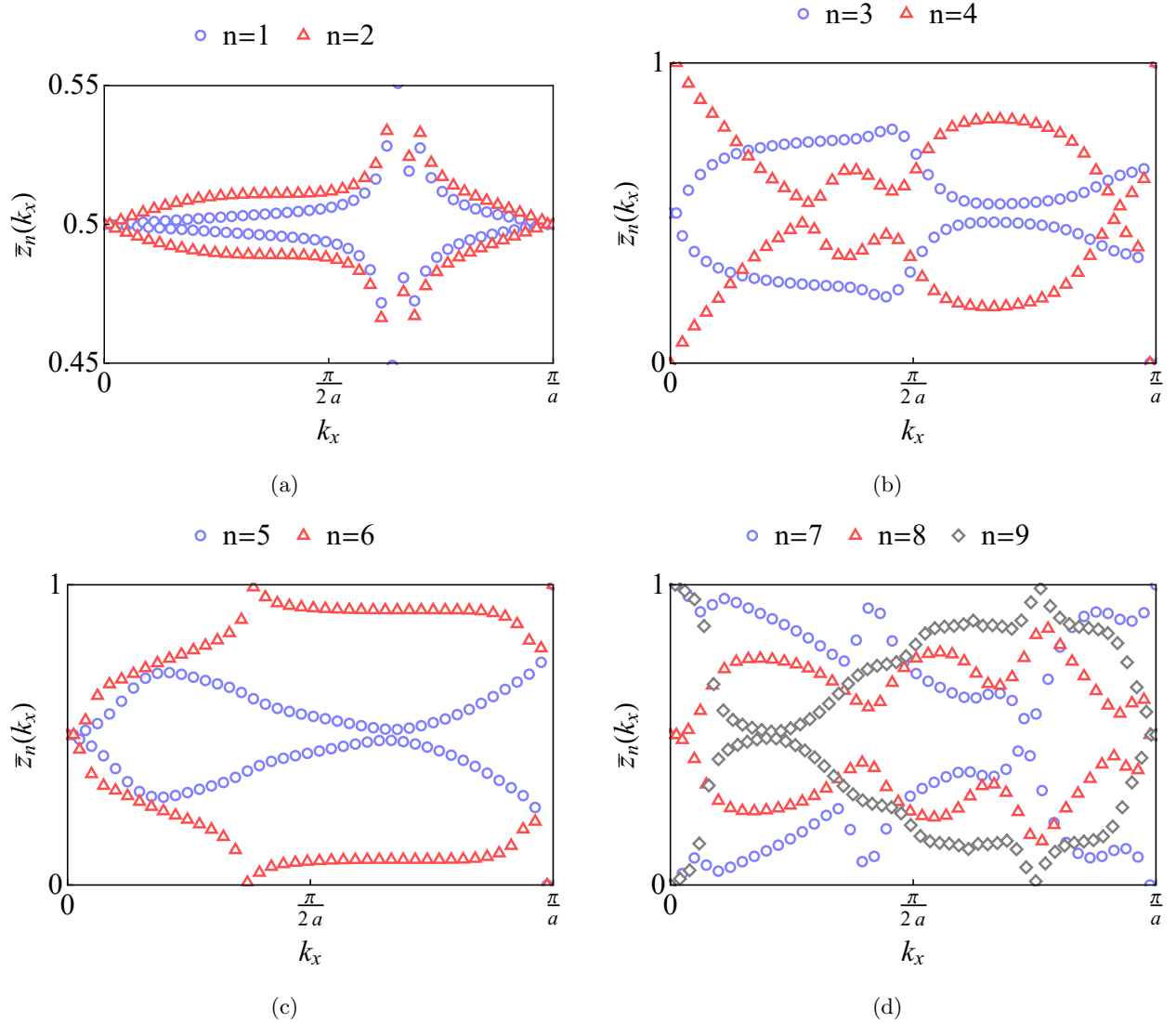


FIG. 10: WCC spectra calculated along k_z as a function of k_x at $k_y = 0$ for each Kramers pair. Bands 3, 5, 6, and 9 (Class A) are fully connected, displaying interpolation between 0 and 1. The WCC spectra for bands 4 and 7 (Class B) remains gapped at all values of k_x , a trivial result. Bands 1, 2, and 8 (Class C) display gapless points in the WCC spectra at both $k_x = 0$ and $k_x = \pi/a$.

bands support a non-trivial strong index in both planes. On the other hand class A bands support only a single plane with a non-trivial strong TI index. Calculation of the strong index for occupied bands results in $\nu_0 = 0$ for both planes.

To differentiate bands in class B and C, WCCs are calculated along the k_z direction as a function of k_x , $\bar{z}(k_x)$, and displayed in Fig. (10). The topological information conveyed by the WCC spectra can again be sorted by class with class A bands displaying a connected WCC spectra (interpolation between $\bar{z} = 0$ and $\bar{z} = 1$) with a single gapless point suggesting a flux tunneling configuration between trivial and non-trivial

planes. WCC spectra of class B bands are fully gapped suggesting the absence of tunneling, and class C supports two gapless points at high-symmetry locations, allowing for the possibility of tunneling between two non-trivial planes. We now turn to calculation of κ_{AF} , the results of which are visible in Fig. (11a).

It is immediately clear that κ_{AF} substantiates the analysis of the $xy_{\Gamma,T}$ planes. Class A bands return an odd classification as expected due to the existence of a single plane with a non-trivial \mathbb{Z}_2 classification, setting up a flux-tunneling configuration. For class B(C) bands, $\kappa_{AF} = 0(\pm 2)$ is in alignment with prior analysis of TB models and the hypothesis that an identical(opposite) parity eigenvalue configuration in the $xy_{\Gamma,T}$ planes indicate flux tunneling is absent(present).

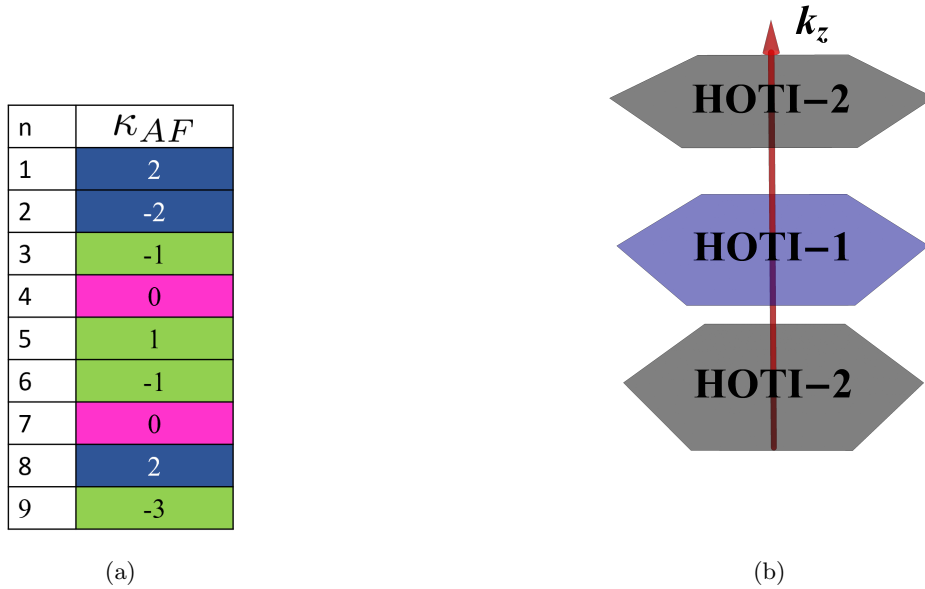


FIG. 11: (a) Assignment of anti-ferromagnetic index to the Kramers degenerate bands of Bi. The bands are color coded according to whether they belong to class A (green), B (purple), or C (blue), as described in the main text. (b) Schematic detailing topological nature of high symmetry hexagonal planes along (111) axis. The xy planes centered at the Γ and T point, support distinct configurations of quantized non-Abelian flux. The k_z axis (111 axis), thus acts as a tunneling configuration between topologically distinct insulators.

In terms of effects on physical observables, we emphasize the fact that Bi supports electron/hole pockets; the presence of such fractional occupations leads to the prediction that realistic samples of elemental Bismuth support non-quantized, but non-zero Chern-Simons invariant leading to an electromagnetic response. A future direction of this work will be to assign definitive signs to n_3 in *Ab initio* systems; which requires developing a methodology by which non-Abelian flux can be determined with a definitive sign without the requirement of mirror symmetry.

IV. APPLICATION OF ANTI-FERROMAGNETIC INDEX TO SB, P AND Bi_2Se_3

Upon performing a thorough investigation of Bi, we now focus our attention on application of κ_{AF} to three further materials of current experimental interest in space group 166, antimony (Sb), phosphorus (P), and bismuth selenide (Bi_2Se_3). For each material we calculate the bulk band structure following the same procedure utilized for Bi, and identify the parity eigenvalues at each TRIM location. This information is then used to calculate κ_1 , the weak TI indices, and κ_{AF} . The bands are color coded following the same scheme used for Bi, with black bands indicating a parity monopole configuration.

Antimony:

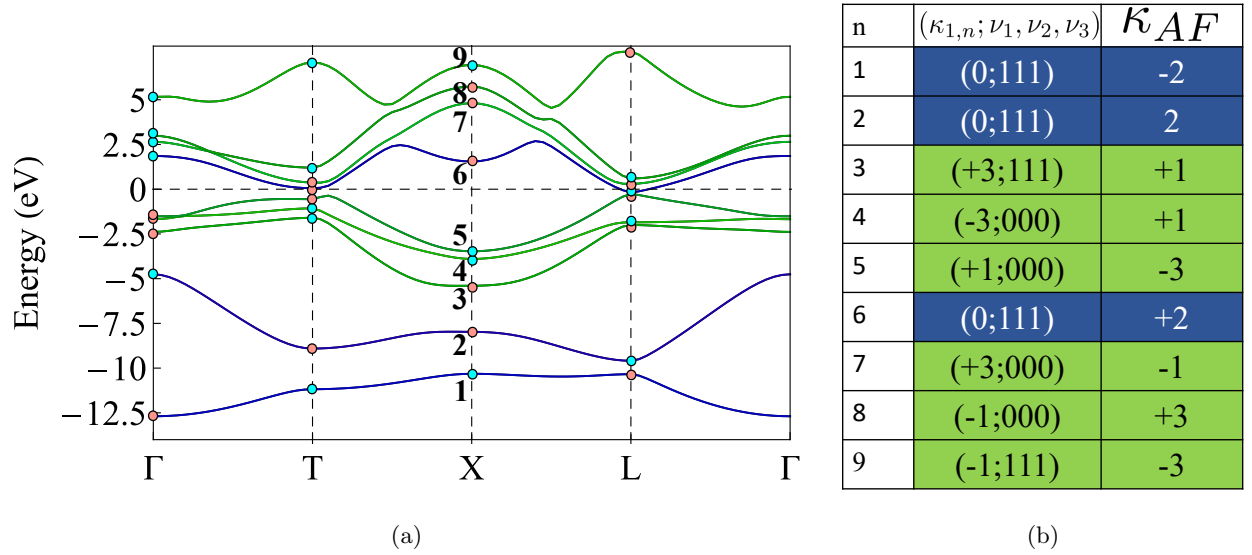


FIG. 12: Bulk band structure of Sb for COD entry 9008575, with parity eigenvalues at TRIM points detailed by cyan and light red circles. If we consider the five lowest lying bands as the occupied bands, Sb is classified as a strong topological insulator due to the presence of three bands supporting a non-trivial strong TI (STI) classification^{7,57}. Nevertheless, we note that κ_1 is not sensitive to the non-trivial topology of bands 1, 2 and 6. Each of these bands admits an even κ_{AF} , indicating an even third-homotopy classification. As in Bi, we conclude that all bands of Sb are topologically non-trivial.

Phosphorus:

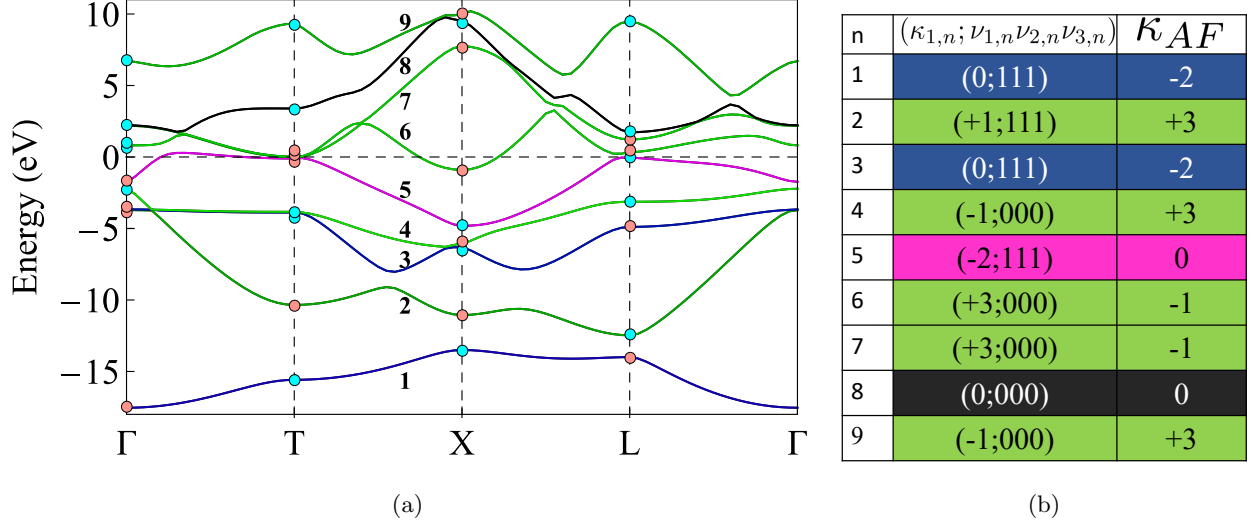


FIG. 13: Bulk band structure of P for ICSD entry 53301, with parity eigenvalues labeled. We note that, as is the case in Bi, if the five lowest lying bands are considered as the occupied ground state, the ground state is assigned $\kappa_1 = -2$, with this classification being due to band 5 rather than the presence of bands 2 and 4 admitting a non-trivial STI classification¹⁹. Unlike Bi or Sb, P supports a single band which has a parity monopole configuration with trivial κ_1 and κ_{AF} .

Bi₂Se₃:

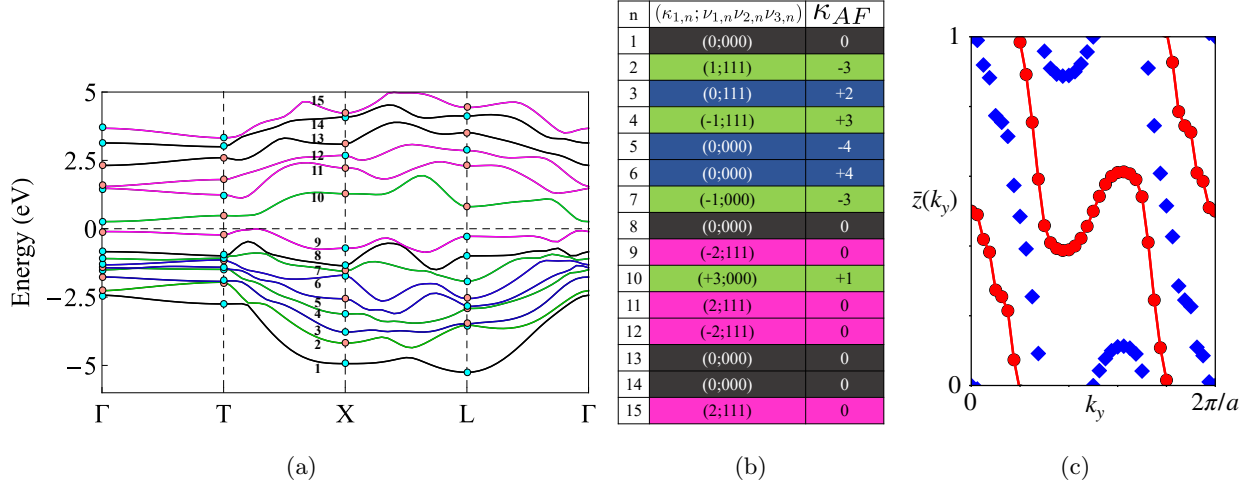


FIG. 14: Bulk band structure of Bi_2Se_3 for COD entry 9011965. This material has been extensively studied as one of the preeminent examples of a topological insulator^{67,68}. Classification of the ground states as an STI is clear as there exists three bands below the Fermi energy which admit a non-trivial strong TI invariant. Taking a band-wise approach, we note that Bi_2Se_3 admits all band types found in Bi, Sb, and P, as well as multiple bands (5 and 6), which follow the configuration displayed for phase IX in Fig. (3b), i.e. trivial κ_1 and weak indices, with a non-trivial κ_{AF} . These bands are of particular interest as they have been overlooked entirely by current symmetry indicator methods. (c) In accordance with a maximal third-homotopy, we must be able to identify planes supporting quantized flux, the YZ mirror planes in this case. Calculation of mirror Chern number for band 6 in the $k_x = 0$ plane for the $+i$ eigenstates of the mirror operator is detailed using Z2Pack. Blue rhombi quantify largest gap of WCCs and red circles track sum of WCCs. The result $n_m = -2$ is the maximum possible result for the C_2 symmetric plane and in accordance with a maximal value for κ_{AF} .

V. SUMMARY

In closing, symmetry indicator methods have proven invaluable for diagnosing topological order in complicated systems of many bands. Our work details that κ_1 quantifies the net ferromagnetic moment of parity eigenvalues. As such, κ_1 and weak \mathbb{Z}_2 indices are unable to diagnose the presence of even integer bulk winding numbers. The use of κ_{AF} offers a computationally efficient way of categorizing individual bands possessing even, odd, and vanishing winding numbers.

Our work calls for a reexamination of the multiple topological material databases to account for: (1) the distinction between bands yielding $\kappa_1 = 0$ before and after imposing the \mathbb{Z}_4 condition, and (2) assignment of κ_{AF} . To complete this work and allow for exact determination of third-homotopy class with a definitive sign for each Kramers pair, advanced computational techniques for gauge-fixing must be implemented. This is particularly challenging and computationally expensive for *Ab initio* data, and will be pursued in future works.

ACKNOWLEDGMENTS

This work was supported by the National Science Foundation MRSEC program (DMR-1720319) at the Materials Research Center of Northwestern University, and the start up funds of P. G. provided by the Northwestern University. A part of this work was performed at the Aspen Center for Physics, which is supported by National Science Foundation grant PHY-1607611.

VI. METHODS

The non-Abelian Berry's gauge connection for each Kramer's pair is an $SU(2)$ object. As the basis for the simplified TB model of (11) is defined such that C_{3z} is a diagonal matrix, we recognize that the $U(1)$, Abelianized component falls on the third color component of the matrix values Berry's connection for each Kramers pair³³. In order to then isolate the corresponding Abelianized curvature originating from this color component we first break the Kramers degeneracy by introducing the, diagonal, traceless matrix $\Gamma_{NA} = \sigma_3 \otimes \sigma_3 \otimes \sigma_3$, such that $H(\mathbf{k}) \rightarrow H(\mathbf{k}) + \alpha \Gamma_{NA}$. Γ_{NA} then serves to break the Kramers degeneracy, separating the Kramer's pairs in energy by $|2\alpha|$ at the zone center. Taking the limit, $\alpha \rightarrow 0$, the Kramers degenerate limit, we then calculate the Abelianized curvature as⁶⁹,

$$\theta_m = \int_{BZ} d\mathbf{k} \sum_{n \neq m} 2\text{Im} \frac{\langle \psi_{n,\mathbf{k}} | \frac{\partial \hat{H}}{\partial k_x} | \psi_{m,\mathbf{k}} \rangle \langle \psi_{m,\mathbf{k}} | \frac{\partial \hat{H}}{\partial k_y} | \psi_{n,\mathbf{k}} \rangle}{(E_{m,\mathbf{k}} - E_{n,\mathbf{k}})^2}, \quad (19)$$

where $E_{m,\mathbf{k}}$ is the energy of band m . In order to assign a definitive sign to the relative Chern number of each Kramers pair, we fix the sign to that of the higher energy state upon breaking the degeneracy with $\alpha \neq 0$.

-
- ¹ C. L. Kane and E. J. Mele, *Phys. Rev. Lett.* **95**, 146802 (2005).
 - ² B. A. Bernevig, T. L. Hughes, and S.-C. Zhang, *Science* **314**, 1757 (2006).
 - ³ L. Fu, C. L. Kane, and E. J. Mele, *Phys. Rev. Lett.* **98**, 106803 (2007).
 - ⁴ J. E. Moore and L. Balents, *Phys. Rev. B* **75**, 121306 (2007).
 - ⁵ R. Roy, *Phys. Rev. B* **79**, 195321 (2009).
 - ⁶ X.-L. Qi, T. L. Hughes, and S.-C. Zhang, *Phys. Rev. B* **78**, 195424 (2008).
 - ⁷ L. Fu and C. L. Kane, *Phys. Rev. B* **76**, 045302 (2007).
 - ⁸ S. Ryu, A. P. Schnyder, A. Furusaki, and A. W. Ludwig, *New J. Phys.* **12**, 065010 (2010).
 - ⁹ M. Z. Hasan and C. L. Kane, *Rev. Mod. Phys.* **82**, 3045 (2010).
 - ¹⁰ X.-L. Qi and S.-C. Zhang, *Rev. Mod. Phys.* **83**, 1057 (2011).
 - ¹¹ C.-K. Chiu, J. C. Y. Teo, A. P. Schnyder, and S. Ryu, *Rev. Mod. Phys.* **88**, 035005 (2016).
 - ¹² E. Khalaf, H. C. Po, A. Vishwanath, and H. Watanabe, *Phys. Rev. X* **8**, 031070 (2018).
 - ¹³ B. Bradlyn, L. Elcoro, J. Cano, M. Vergniory, Z. Wang, C. Felser, M. Aroyo, and B. A. Bernevig, *Nature* **547**, 298 (2017).
 - ¹⁴ H. C. Po, A. Vishwanath, and H. Watanabe, *Nat. Comms.* **8**, 1 (2017).
 - ¹⁵ J. Cano, B. Bradlyn, Z. Wang, L. Elcoro, M. G. Vergniory, C. Felser, M. I. Aroyo, and B. A. Bernevig, *Phys. Rev. B* **97**, 035139 (2018).
 - ¹⁶ M. Vergniory, L. Elcoro, C. Felser, N. Regnault, B. A. Bernevig, and Z. Wang, *Nature* **566**, 480 (2019).
 - ¹⁷ T. Zhang, Y. Jiang, Z. Song, H. Huang, Y. He, Z. Fang, H. Weng, and C. Fang, *Nature* **566**, 475 (2019).
 - ¹⁸ F. Tang, H. C. Po, A. Vishwanath, and X. Wan, *Nat. Phys.* **15**, 470 (2019).
 - ¹⁹ F. Tang, H. C. Po, A. Vishwanath, and X. Wan, *Nature* **566**, 486 (2019).
 - ²⁰ M. G. Vergniory, B. J. Wieder, L. Elcoro, S. S. Parkin, C. Felser, B. A. Bernevig, and N. Regnault, *arXiv:2105.09954* (2021).
 - ²¹ Y. Xu, L. Elcoro, Z.-D. Song, B. J. Wieder, M. Vergniory, N. Regnault, Y. Chen, C. Felser, and B. A. Bernevig, *Nature* **586**, 702 (2020).
 - ²² L. Elcoro, B. J. Wieder, Z. Song, Y. Xu, B. Bradlyn, and B. A. Bernevig, *arXiv:2010.00598* (2020).
 - ²³ R. Yu, X. L. Qi, A. Bernevig, Z. Fang, and X. Dai, *Phys. Rev. B* **84**, 075119 (2011).
 - ²⁴ A. Alexandradinata, X. Dai, and B. A. Bernevig, *Phys. Rev. B* **89**, 155114 (2014).
 - ²⁵ M. Taherinejad, K. F. Garrity, and D. Vanderbilt, *Phys. Rev. B* **89**, 1 (2014), 1312.6940.
 - ²⁶ D. Gresch, G. Autès, O. V. Yazyev, M. Troyer, D. Vanderbilt, B. A. Bernevig, and A. A. Soluyanov, *Phys. Rev. B* **95**, 075146 (2017).
 - ²⁷ A. A. Soluyanov and D. Vanderbilt, *Phys. Rev. B* **83**, 235401 (2011).
 - ²⁸ A. Bouhon, A. M. Black-Schaffer, and R.-J. Slager, *Phys. Rev. B* **100**, 195135 (2019).
 - ²⁹ B. Bradlyn, Z. Wang, J. Cano, and B. A. Bernevig, *Phys. Rev. B* **99**, 045140 (2019).
 - ³⁰ D. S. Freed and G. W. Moore, in *Ann. Henri Poincaré*, Vol. 14 (Springer, 2013) pp. 1927–2023.
 - ³¹ N. Okuma, M. Sato, and K. Shiozaki, *Phys. Rev. B* **99**, 085127 (2019).
 - ³² F. Schindler, A. M. Cook, M. G. Vergniory, Z. Wang, S. S. Parkin, B. A. Bernevig, and T. Neupert, *Sci. Adv.* **4** (2018), 10.1126/sciadv.aat0346.
 - ³³ A. C. Tyner, S. Sur, D. Puggioni, J. M. Rondinelli, and P. Goswami, *arXiv:2012.12906* (2020).

- ³⁴ A. C. Tyner, S. Sur, Q. Zhou, D. Puggioni, P. Darancet, J. M. Rondinelli, and P. Goswami, arXiv:2102.06207 (2021).
- ³⁵ A. M. Essin, J. E. Moore, and D. Vanderbilt, *Phys. Rev. Lett.* **102**, 146805 (2009).
- ³⁶ M. Z. Hasan and J. E. Moore, *Annu. Rev. Condens. Matter Phys.* **2**, 55 (2011).
- ³⁷ F. Schindler, Z. Wang, M. G. Vergniory, A. M. Cook, A. Murani, S. Sengupta, A. Y. Kasumov, R. Deblock, S. Jeon, I. Drozdov, *et al.*, *Nat. Phys.* **14**, 918 (2018).
- ³⁸ A. Malashevich, I. Souza, S. Coh, and D. Vanderbilt, *New J. Phys.* **12**, 053032 (2010).
- ³⁹ S. Coh, D. Vanderbilt, A. Malashevich, and I. Souza, *Phys. Rev. B* **83**, 085108 (2011).
- ⁴⁰ N. Varnava, I. Souza, and D. Vanderbilt, *Phys. Rev. B* **101**, 155130 (2020).
- ⁴¹ Y. Liu and R. E. Allen, *Phys. Rev. B* **52**, 1566 (1995).
- ⁴² J. C. Teo, L. Fu, and C. Kane, *Phys. Rev. B* **78**, 045426 (2008).
- ⁴³ D. Hsieh, D. Qian, L. Wray, Y. Xia, Y. S. Hor, R. J. Cava, and M. Z. Hasan, *Nature* **452**, 970 (2008).
- ⁴⁴ A. N. Rudenko, M. I. Katsnelson, and R. Roldán, *Phys. Rev. B* **95**, 081407 (2017).
- ⁴⁵ S. H. Kim, K.-H. Jin, J. Park, J. S. Kim, S.-H. Jhi, and H. W. Yeom, *Sci. Rep.* **6**, 1 (2016).
- ⁴⁶ S.-Y. Zhu, Y. Shao, E. Wang, L. Cao, X.-Y. Li, Z.-L. Liu, C. Liu, L.-W. Liu, J.-O. Wang, K. Ibrahim, *et al.*, *Nano Lett.* **19**, 6323 (2019).
- ⁴⁷ M. Bieniek, T. Woźniak, and P. Potasz, *J. Condens. Matter Phys.* **29**, 155501 (2017).
- ⁴⁸ C.-H. Hsu, X. Zhou, T.-R. Chang, Q. Ma, N. Gedik, A. Bansil, S.-Y. Xu, H. Lin, and L. Fu, *Proc. Natl. Acad. Sci.* **116**, 13255 (2019).
- ⁴⁹ P. Hofmann, *Prog. Surf. Sci.* **81**, 191 (2006).
- ⁵⁰ M. Wada, S. Murakami, F. Freimuth, and G. Bihlmayer, *Phys. Rev. B* **83**, 121310 (2011).
- ⁵¹ B. Rasche, A. Isaeva, M. Ruck, S. Borisenko, V. Zabolotnyy, B. Büchner, K. Koepernik, C. Ortix, M. Richter, and J. Van Den Brink, *Nat. Mater.* **12**, 422 (2013).
- ⁵² I. K. Drozdov, A. Alexandradinata, S. Jeon, S. Nadj-Perge, H. Ji, R. Cava, B. A. Bernevig, and A. Yazdani, *Nat. Phys.* **10**, 664 (2014).
- ⁵³ L. Chen, Z. F. Wang, and F. Liu, *Phys. Rev. B* **87**, 235420 (2013).
- ⁵⁴ A. K. Nayak, J. Reiner, R. Queiroz, H. Fu, C. Shekhar, B. Yan, C. Felser, N. Avraham, and H. Beidenkopf, *Sci. Adv.* **5**, eaax6996 (2019).
- ⁵⁵ A. Takayama, T. Sato, S. Souma, T. Oguchi, and T. Takahashi, *Phys. Rev. Lett.* **114**, 066402 (2015).
- ⁵⁶ T. Lei, K.-H. Jin, N. Zhang, J.-L. Zhao, C. Liu, W.-J. Li, J.-O. Wang, R. Wu, H.-J. Qian, F. Liu, *et al.*, *J. Condens. Matter Phys.* **28**, 255501 (2016).
- ⁵⁷ T.-R. Chang, Q. Lu, X. Wang, H. Lin, T. Miller, T.-C. Chiang, and G. Bian, *Crystals* **9**, 510 (2019).
- ⁵⁸ S. Ito, B. Feng, M. Arita, A. Takayama, R.-Y. Liu, T. Someya, W.-C. Chen, T. Iimori, H. Namatame, M. Taniguchi, C.-M. Cheng, S.-J. Tang, F. Komori, K. Kobayashi, T.-C. Chiang, and I. Matsuda, *Phys. Rev. Lett.* **117**, 236402 (2016).
- ⁵⁹ K. Saito, H. Sawahata, T. Komine, and T. Aono, *Phys. Rev. B* **93**, 041301 (2016).
- ⁶⁰ S. Golin, *Phys. Rev.* **166**, 643 (1968).
- ⁶¹ A. Jain, S. P. Ong, G. Hautier, W. Chen, W. D. Richards, S. Dacek, S. Cholia, D. Gunter, D. Skinner, G. Ceder, and K. A. Persson, *APL Materials* **1**, 011002 (2013).
- ⁶² P. Giannozzi, S. Baroni, N. Bonini, M. Calandra, R. Car, C. Cavazzoni, D. Ceresoli, G. L. Chiarotti, M. Cococcioni, I. Dabo, A. Dal Corso, S. de Gironcoli, S. Fabris, G. Fratesi, R. Gebauer, U. Gerstmann, C. Gougoussis, A. Kokalj,

- M. Lazzeri, L. Martin-Samos, N. Marzari, F. Mauri, R. Mazzarello, S. Paolini, A. Pasquarello, L. Paulatto, C. Sbraccia, S. Scandolo, G. Sciauzero, A. P. Seitsonen, A. Smogunov, P. Umari, and R. M. Wentzcovitch, *J. Phys. Condens. Matter* **21**, 395502 (19pp) (2009).
- ⁶³ P. Giannozzi, O. Andreussi, T. Brumme, O. Bunau, M. B. Nardelli, M. Calandra, R. Car, C. Cavazzoni, D. Ceresoli, M. Cococcioni, N. Colonna, I. Carnimeo, A. D. Corso, S. de Gironcoli, P. Delugas, R. A. D. Jr, A. Ferretti, A. Floris, G. Fratesi, G. Fugallo, R. Gebauer, U. Gerstmann, F. Giustino, T. Gorni, J. Jia, M. Kawamura, H.-Y. Ko, A. Kokalj, E. Küçükbenli, M. Lazzeri, M. Marsili, N. Marzari, F. Mauri, N. L. Nguyen, H.-V. Nguyen, A. O. de-la Roza, L. Paulatto, S. Poncé, D. Rocca, R. Sabatini, B. Santra, M. Schlipf, A. P. Seitsonen, A. Smogunov, I. Timrov, T. Thonhauser, P. Umari, N. Vast, X. Wu, and S. Baroni, *J. Phys. Condens. Matter* **29**, 465901 (2017).
- ⁶⁴ P. Giannozzi, O. Baseggio, P. Bonfà, D. Brunato, R. Car, I. Carnimeo, C. Cavazzoni, S. de Gironcoli, P. Delugas, F. Ferrari Ruffino, A. Ferretti, N. Marzari, I. Timrov, A. Urru, and S. Baroni, *J. Chem. Phys.* **152**, 154105 (2020).
- ⁶⁵ J. P. Perdew, K. Burke, and M. Ernzerhof, *Phys. Rev. Lett.* **77**, 3865 (1996).
- ⁶⁶ G. Pizzi, V. Vitale, R. Arita, S. Blugel, F. Freimuth, G. Géranton, M. Gibertini, D. Gresch, C. Johnson, T. Koretsune, J. Ibañez-Azpiroz, H. Lee, J.-M. Lihm, D. Marchand, A. Marrazzo, Y. Mokrousov, J. I. Mustafa, Y. Nohara, Y. Nomura, L. Paulatto, S. Poncé, T. Ponweiser, J. Qiao, F. Thole, S. S. Tsirkin, M. Wierzbowska, N. Marzari, D. Vanderbilt, I. Souza, A. A. Mostofi, and J. R. Yates, *J. Phys. Condens. Matter* **32**, 165902 (2020).
- ⁶⁷ H. Zhang, C.-X. Liu, X.-L. Qi, X. Dai, Z. Fang, and S.-C. Zhang, *Nat. Phys.* **5**, 438 (2009).
- ⁶⁸ Y. Xia, D. Qian, D. Hsieh, L. Wray, A. Pal, H. Lin, A. Bansil, D. Grauer, Y. S. Hor, R. J. Cava, *et al.*, *Nat. Phys.* **5**, 398 (2009).
- ⁶⁹ D. J. Thouless, M. Kohmoto, M. P. Nightingale, and M. den Nijs, *Phys. Rev. Lett.* **49**, 405 (1982).